

## **Polarimetric imaging system for automatic target detection and recognition**

March 2000

Cornell S.L. Chun  
Physics Innovations Inc.  
P.O. Box 2171, Inver Grove Heights, MN 55076-8171

Firooz A. Sadjadi  
Lockheed Martin Corp.  
P.O. Box 64525, St. Paul, MN 55164-0525

### **ABSTRACT**

When thermal imaging sensors are used for automatic target detection and recognition of ground targets, the performance is often limited by the small thermal contrast between target and background. In comparison, polarimetric imaging is minimally dependent on the thermal characteristics of the target. Polarimetric data depends, instead, on the three-dimensional shape and surface properties of the target. Physics Innovations Inc. and Lockheed Martin Corp. have an ongoing program to develop polarimetric imaging systems for automatic target detection and recognition. In this paper, we will discuss two novel technologies which we have recently developed for these imaging systems. The first is a two-dimensional array of microscale retarders. This retarder array, when combined with a two-dimensional array of linear polarizers and a focal plane array, will enable the imaging of the four Stokes parameters at video frame rates without the mechanical rotation of optical components. The retarder elements are highly achromatic. Furthermore, the retarders have a large field angle. A large field angle will facilitate the use of low f-number optics for greater sensitivity. The second technology developed for polarimetric imaging systems are target detection and recognition algorithms which optimally combine the Stokes images.

## **1. POLARIZATION-SENSITIVE THERMAL IMAGING**

### **1.1. POLARIZED THERMAL EMISSION AND SURFACE ORIENTATION**

Conventional methods for passively detecting and identifying targets often rely on sensing the intensity of infrared light reflected or emitted by objects. A fundamental problem associated with sensing the intensity is that intensity gives one parameter while the orientation of surface elements has two degrees of freedom. Physics Innovations Inc. has developed a thermal imaging technique for determining surface orientation where, in each image pixel, two parameters are sensed simultaneously. The two parameters, percent of polarization  $P$  and angle of the plane of polarization  $\phi$  are directly related to the two angles of surface orientation. Although thermal infrared intensity images of terrestrial scenes have low contrast, images of  $P$

## Report Documentation Page

<b>Report Date</b> 00032000	<b>Report Type</b> N/A	<b>Dates Covered (from... to)</b> -
<b>Title and Subtitle</b> Polarimetric imaging system for automatic target detection and recognition	<b>Contract Number</b>	
	<b>Grant Number</b>	
	<b>Program Element Number</b>	
<b>Author(s)</b> Chun, Cornell, S.L.; Sadjadi, Firooz A.	<b>Project Number</b>	
	<b>Task Number</b>	
	<b>Work Unit Number</b>	
<b>Performing Organization Name(s) and Address(es)</b> Physics Innovations Inc. P.O. Box 2171 Inver Grove Heights, MN 55076-8171	<b>Performing Organization Report Number</b>	
<b>Sponsoring/Monitoring Agency Name(s) and Address(es)</b> Director, CECOM RDEC Night Vision and Electronic Sensors Directorate, Security Team 10221 Burbeck Road Ft. Belvoir, VA 22060-5806	<b>Sponsor/Monitor's Acronym(s)</b>	
	<b>Sponsor/Monitor's Report Number(s)</b>	
<b>Distribution/Availability Statement</b> Approved for public release, distribution unlimited		
<b>Supplementary Notes</b> The original document contains color images.		
<b>Abstract</b>		
<b>Subject Terms</b>		
<b>Report Classification</b> unclassified	<b>Classification of this page</b> unclassified	
<b>Classification of Abstract</b> unclassified	<b>Limitation of Abstract</b> UNLIMITED	
<b>Number of Pages</b> 19		

and  $\phi$  often have high contrast for different surface orientations. This high contrast should facilitate image segmentation and classification of objects.

Polarization also gives useful information about the surface properties of the object. Man-made objects have unnaturally smooth surfaces, leading to radiation with greater polarization. Natural backgrounds such as grass, trees, dirt, and sand emit and reflect radiation that is less polarized.

Researchers have recognized the potential usefulness of imaging polarization data for target detection and recognition. However, wide-spread use of polarization data in the infrared has not occurred, probably because polarization-sensitive imaging methods have been slow, bulky, and subject to object misregistration. Physics Innovations Inc. is developing polarization-sensitive imaging sensors which are compact, portable, and, for some applications, can be retrofitted into existing optical imaging systems.

In this section, we describe the operation of polarization-sensitive thermal imaging sensors which are capable of simultaneously capturing intensity and polarization data without misregistration and in real time. The results show that three-dimensional information, in addition to temperature distribution, can be captured and displayed in real time and at video frequency. These results also show that polarization data provides useful contrast, enough to distinguish man-made objects from backgrounds and to distinguish different surface orientations.

In Section 2, we describe a modification to our method of polarization-sensitive thermal imaging. With this modification, images of circular polarization can be captured. Polarimetric imaging is often proposed as a technique to improve target detection and recognition.

In Section 3 we describe our investigation into the improvement in performance of automatic target recognition algorithms when processing polarimetric images compared to FLIR images.

Polarized thermal emission can be explained by relating to the more common experience of polarized reflection. When light is incident at a grazing angle on the surface of water the portion of the light which is reflected, as in sun glint, is linearly polarized with a horizontal plane of polarization. (Polarizers in sunglasses are oriented to attenuate horizontally polarized light.) The portion of the light which is transmitted into the water is linearly polarized with a vertical plane of polarization. By the same mechanism, if light originates below the surface and passes through the surface, the transmitted light would be linearly polarized with a vertical polarization plane. The polarization plane contains the normal vector to the surface. The transmitted light when exiting at a more grazing angle to the surface will have a greater percent of polarization.

Thermal emission is light originating below the surface. Referring to Figure 1, when thermal radiation is received by a polarization-sensitive sensor from a surface element on an object, the plane of polarization gives the angle  $\phi$  and the percent of polarization  $P$  can be related to the angle  $\theta$ . For most materials,  $P$  increases as  $\theta$  increases [Figure 2]. Together  $\theta$  and  $\phi$  determine the normal vector to the surface element.

## **1.2. IMAGING OF STOKES PARAMETERS**

A beam of incoherent radiation emitted or reflected from a target's surface can be completely described at a given wavelength by the four Stokes parameters, (I, Q, U, V). The first Stokes parameter I is a measure of the total intensity of radiation. The second parameter Q measures the amount of linear polarization in the horizontal direction. The third parameter U measures the amount of linear polarization in a plane rotated 45 degrees from the horizontal.

The fourth parameter V is associated with the circular polarization. A method for imaging V is described in Section 2.

The first three Stokes parameters can be transformed into percent of polarization P and angle of polarization  $\phi$  using the relations,<sup>1</sup>

$$\begin{aligned} P &= \frac{\sqrt{Q^2 + U^2}}{I} * 100 \\ \phi &= \frac{1}{2} * \arctan\left(\frac{U}{Q}\right) \end{aligned} \quad (1)$$

Conventional methods of determining polarization from images rely on the use of a single polarizer covering the entire imaging sensor. In one method, a sequence of four images is taken with a linear polarizer oriented at 0°, 45°, 90°, and 135°. This method can determine the first three of the Stokes parameters at each image pixel:

$$\begin{aligned} I &= \frac{1}{2} * (i_0 + i_{45} + i_{90} + i_{135}) \\ Q &= i_0 - i_{90} \\ U &= i_{45} - i_{135} \end{aligned} \quad (2)$$

where  $i_x$  is the intensity measured with the polarizer oriented at x degrees. These equations assume that the polarizers are ideal, i.e. 100% transmittance for radiation linearly polarized at angle x and zero transmittance for radiation at angle x + 90°. The effects of non-ideal polarizers are discussed in Reference 1.

### 1.3. METHOD OF IMAGING INTENSITY AND POLARIZATION IN A SINGLE VIDEO FRAME

In an imaging sensor developed at Physics Innovations Inc., each detector element has its own polarizer and the polarizer orientations are rotated from element to element. Referring to Figure 3, the Stokes parameters characterizing radiation emitted and reflected from the part of an object imaged onto detector elements A, B, C, and D can be determined by using the Equations (2). The accuracy of this measurement assumes that the intensity and polarization state does not vary significantly over A, B, C, and D. This assumption is satisfied if detector elements A, B, C, and D see only a localized part of an object. Localized measurements can be made if the detector array has high spatial resolution relative to the overall dimensions of the object. (This assumption is not necessary when using the technique described in the next section.)

Wire grid polarizers can be integrated with photodiode arrays by placing the polarizers on a substrate in close proximity to the photodiode array [Figure 4(a)]. The optimum arrangement would have the polarizer array formed on the same substrate as the photodetector focal plane array, i.e. a monolithic integration. For the purpose of demonstrating the feasibility of using polarizer arrays, a more convenient method of integrating the polarizer array with a thermal imaging sensor is shown schematically in Figure 4(b). Light from the target is imaged by an objective lens onto the polarizer array. The light, which is transmitted through the polarizers, is imaged using a relay lens onto the thermal imaging sensor, here a focal plane array. In the work described in this paper, the focal plane array camera was a Mitsubishi IR-M300

Thermal Imager. The Mitsubishi camera has a 256x256 PtSi array and is sensitive to radiation in the 3 to 5 micron region (MWIR). The technique shown in Figure 4(b) can also be used to integrate polarizer arrays with other types of imaging sensors, such as LWIR cameras and uncooled focal plane arrays.

Figure 5 is an image of a heated cube which is used as a target. A single video frame was captured from the output of the Mitsubishi camera. A computer program was written which takes the video frame and calculates the Stokes parameters I, P, and  $\phi$  using Equations (1) and (2).

#### 1.4. METHOD OF IMAGING INTENSITY AND POLARIZATION IN A SEQUENCE OF VIDEO FRAMES

The above images of intensity and polarization do not have the full spatial resolution of the focal plane camera, 256 x 256 for the Mitsubishi M300 camera. The full spatial resolution can be achieved by microscanning the image over the polarizer array. As shown in Figure 7, first a video frame is captured, then the image is displaced horizontally and a second video frame is captured. The image is displaced vertically and a third video frame is captured. From these three video frames, the Stokes parameters can be calculated. For radiation from a point source imaged onto the circle in Figure 7(a) the Stokes parameters are

$$\begin{aligned} I &= i_{45} + i_{135} \\ Q &= (-2 \cdot i_{90}) + i_{45} + i_{135} \\ U &= i_{45} - i_{135} \end{aligned}$$

Using Equations (1), images of I, P, and  $\phi$  can be calculated.

To microscan the image, we used two tilted plane-parallel plates each driven by a stepping motor. One plate and motor were used for horizontal displacement, and the other plate and motor for vertical displacement. The motors were combined with a microstepper driver for sub-pixel resolution and an indexer/controller which interfaces with a personal computer. The motor can rotate a plate by a few degrees in less than 1/60 sec which is a frame time for the Mitsubishi thermal imager. With high-speed digital signal processors, we should be able to capture the sequence of three frames in about 6·1/60 sec. However, in the prototype sensor, such processors were not available, and the three frames were captured in about 3 sec.<sup>2</sup>

Using the microscanning method, we captured polarization data on a die-cast metal scale model of an aircraft [Figure 6]. The model is painted a flat black and heated to about 40C. The intensity I image shows the temperature distribution over the target and is identical to an image from a FLIR sensor. The P image shows significant polarization (bright pixels) over the surfaces which are viewed at a grazing angle. Surfaces facing the sensor, around the nose of the aircraft, have lower percent of polarization (darker pixels). Darker pixels are also seen below the V-shaped tail. This is probably due to radiation emitted by the tail and reflected off the body of the aircraft. When reflected and emitted radiation are combined, the percent of polarization is reduced from that of emission alone.

In the image of the angle of polarization  $\phi$ , surfaces which face the observer's right are dark gray and surfaces facing the observer's left are light gray [Figure 6]. The vertical stripe pattern in this  $\phi$  image is caused by nonuniformities in the particular polarizer array used.

## 2. CIRCULAR POLARIZATION IMAGING USING AN ACHROMATIC RETARDER ARRAY

### 2.1. ACHROMATIC QUARTER-WAVE RETARDER

The sensor described in the previous section is capable of imaging three Stokes parameters. In order to extend the sensor's capabilities to image all four Stokes parameters I, Q, U, and V, we are developing novel microscale retarder arrays. In an imaging sensor, each retarder element will be combined with a linear polarizer element. This sensor will be able to capture images of the four Stokes parameters in real time and without mechanically moving parts. The waveplates and polarizers can be fabricated using conventional microlithography.

A well-established method for constructing an achromatic quarter-wave retarder is to use a combination of a quarter-wave waveplate followed by a half-wave waveplate<sup>3</sup>. In Figure 8(a), a Poincare sphere representation shows how the composite retarder transforms right circularly polarized light V to horizontal linearly polarized light Q. The quarter-wave waveplate transforms the circularly polarized component V to linearly polarized component A. The half-wave waveplate then rotates the plane of polarization to change component A to Q. The composite retarder is achromatic. For example, if, at a different wavelength, the magnitude of the birefringence is slightly larger by a factor  $m > 1$ , then, on the Poincare sphere, the component V will be transformed through a path  $m$  times longer to A'. In the half-wave waveplate, the path will also be  $m$  times longer, so A' will be transformed to a point close to Q.

The composite retarder may also have a wider field angle than a single waveplate. If a ray enters the quarter-wave waveplate in a direction normal to the surface, then V will be transformed to A. If another ray is incident at an angle greater than zero, then it travels a longer distance through the waveplate, and V will be transformed to A'. The latter ray will also travel through a longer distance in the half-wave waveplate, and A' will be transformed to a point close to Q.

The composite retarder can be constructed by stacking two waveplates with their fast axes appropriately rotated [Figure 8(b)]. As discussed below, an array of composite retarders can be fabricated on a substrate.

### 2.2. SURFACE-RELIEF GRATINGS

In the sensor described in Section 1, each pixel in a focal plane array has its own microscale linear polarizer. Correspondingly, in order to detect circular polarized light, the linear polarizer in Figure 8(b) has its own microscale composite retarder. The composite retarder is an element in an array of retarders. Each composite retarder can be constructed by stacking two waveplates. The individual waveplates are surface-relief gratings. A grating is a series of identical parallel linear ridges arranged on a planar substrate. As shown in Figure 9, these grooves and ridges constitute a form birefringent material.

We demonstrated that a combination of surface-relief gratings behaves as an achromatic quarter-wave retarder using Mueller matrices.<sup>4</sup> We assume a Si/air layered material for the  $\frac{1}{4}$ -wave and  $\frac{1}{2}$ -wave waveplates. We can calculate the birefringence from effective medium theory.<sup>5</sup> For radiation incident in a direction normal to plane of the surface-relief gratings, the retardance, for radiation with wavelengths from 3 to 5  $\mu\text{m}$ , is shown in Figure 11(a). The retardance is nearly independent of wavelength in the range 3–5  $\mu\text{m}$  with a standard deviation of  $0.626^\circ$ . For comparison, the retardance of a  $\frac{1}{4}$ -wave waveplate made from a single surface relief grating layer is plotted and has a standard deviation of  $12.5^\circ$ .

In our imaging sensor, light will enter the composite retarder in a range of angles [Figure 10(c)]. The field angle required for the composite retarder is determined by the f-number of the objective lens. For example, if  $f/\# = 1.2$ , then maximum field angle is  $22.6^\circ$ . The Mueller matrix calculation, assuming an incidence angle of  $22.6^\circ$  from normal, is shown in Figure 11(b). The retardance has a standard deviation of  $0.712^\circ$  for the composite retarder. We varied the angles of the fast axes [Figure 8(b)], and found that the optimum angles are  $-30.0^\circ$  for the  $1/4$ -wave grating and  $+29.3^\circ$  for the  $1/2$ -wave grating. These are the angles used in Figure 11.

### 2.3. IMAGING FOUR STOKES PARAMETERS

Figure 10 shows how a wide-band Stokes-vector imaging sensor can be constructed by placing the retarder array in close proximity with the wire grid polarizer array in a sandwich structure. Light from the target is focused by an objective lens on the retarder/polarizer arrays. Light which is transmitted by the retarder/polarizer arrays is imaged onto the focal plane array using a relay lens. In Figure 10(a), when array elements A, B, C, D, E, and F view a localized area on the target, then the Stokes images can be captured in a single video frame. The photodetector signals at A, B, C, D, E, and F give the intensities  $i(90^\circ, 0^\circ)$ ,  $i(135^\circ, 0^\circ)$ ,  $i(45^\circ, 0^\circ)$ ,  $i(0^\circ, 0^\circ)$ ,  $i(90^\circ, 90^\circ)$ , and  $i(0^\circ, 90^\circ)$ , respectively, where the first argument is the angle of rotation of the wire grid polarizer and the second is the phase change due to the retarder. For ideal polarizers and retarders, the Stokes parameters are

$$I = i(0,0) + i(90,0)$$

$$Q = i(0,0) - i(90,0)$$

$$U = i(45,0) - i(135,0)$$

$$V = i(0,90) - i(90,90)$$

## 3. ATR ALGORITHM PERFORMANCE IMPROVEMENT USING POLARIMETRIC IMAGING

### 3.1. SYNTHETIC IMAGERY

Images with polarization data are presently available with the sensor developed at Physics Innovations Inc. [Figure 5 and Figure 6]. However, at the time of this Automatic Target Recognition (ATR) study, actual polarization data did not exist, so we generated synthetic images using ray tracing.<sup>6</sup> A publicly available ray-tracing package was modified with additional modules to generate polarization imagery. In this study the target is a tactical missile mounted horizontally on top of a mobile launcher [Figure 12]. The dimensions of this missile and launcher are approximated those of the Russian-built SCUD missile.

The sensor-derived image was generated using the ray tracer program with the sensor noise included. An example of a sensor image is shown in Figure 12. In all the sensor images the background is a planar surface with the same emissivity and the same temperature (300 K) as the surface of the missile and mobile launcher. The sensor characteristics are typical of a PtSi focal plane array camera. For the images discussed in this paper the frame integration time is 33 millisecond, similar to video frequencies.

### 3.2. EDGE DETECTING ALGORITHM

A selection of algorithms for target edge detection, segmentation, and recognition were evaluated using the sensor images and model images generated with the polarization ray-tracing program. The polarization images have three components: intensity  $I$ , percent of polarization  $P$ , and angle of the plane of polarization  $\phi$ . The intensity  $I$  image is the same as would be captured using a FLIR sensor. We demonstrated the advantages of using polarization imagery by comparing the performance of the algorithms on intensity-only (FLIR) data and the performance on a combination of intensity and polarization data.

For edge detection, we used a Sobel operator. The evaluation method can be described as follows. (1) apply the Sobel operator on each channel ( $I$ ,  $P$ , and  $\phi$ ) of the sensor-derived images (2) apply thresholds to each channel of the Sobel images, (3) add (logical OR) the images from each channel to form a single binary image, and (4) make a pixel-by-pixel comparison of this binary image with the image of the true edges. For the case where we evaluate performance on intensity-only (FLIR) data, there is only one channel ( $I$ ). The detection rate is defined as the ratio of the number of true edge pixels detected to the number of actual true edge pixels. The false detection rate is defined as the ratio of the number of pixels labeled as edges which are not true edges to the number of pixels which are not true edges. The performance of the Sobel operator on the sensor images is summarized using receiver-operating-characteristics (ROC) curves [Figure 13] where the edge detection rate is plotted versus the false detection rate. Different points along a ROC curve correspond to different choices of thresholds when labeling pixels as edges.

The performance evaluation showed that polarization data contribute an improvement over most aspect and elevation angles. For example, at  $30^\circ$  elevation angle and aspect angle of  $30^\circ$ , polarization data gives at least 16% improvement in detection probability over intensity-only (FLIR) data alone [Figure 13]. However, this improvement decreases to 4% when the target is viewed from directly overhead. When the target is viewed directly broadside or for front or back views, polarization data does not improve edge detection over FLIR alone.

### 3.3. STATISTICAL SEGMENTATION AND LABELING ALGORITHM

In the statistical segmentation and labeling algorithm, the input consists of the sensor  $I$ ,  $P$ , and  $\phi$  imagery, the estimated size of the targets, and the first and the second order statistics of the objects of the interest. The first and the second order statistics of the regions of the original imagery falling under a moving window of the size specified by the estimated size of the objects of interest are computed. Next a measure of the statistical similarity, the Fisher Criterion  $F$ , between the extracted statistics and the inputted statistics are made. The regions that have statistical similarity to the object's statistics will generate low  $F$  values. This algorithm will produce not only segmentation of the scene but also a classification of them into classes of interest.

The method used to evaluate the performance of this algorithm has the following steps. (1) Apply the statistical segmentation and labeling algorithm to the sensor image. The output is a grayscale image,  $F$  image, where each pixel is labeled with a value  $F$ , a measure of the statistical similarity between the extracted statistics of the sensor image and the statistics of the true image of the target. (2) Threshold the  $F$  image; all pixels with  $F$  less than the threshold are labeled to be target pixels. (3) Compare pixel-by-pixel the thresholded  $F$  image with the model image containing the true target region. The results of the comparison are described in terms of

segmentation accuracy and false detection rate. Segmentation accuracy is defined as the ratio of the number of pixels in the set ( $L \cap T$ ) to the number of pixels in the set ( $L \cup T$ ), where  $L$  is the set of pixels labeled to be target pixels and  $T$  is the set of pixels in the true target region. False detection rate is defined as the ratio of the number of pixels labeled to be target pixels which are not in the true target region to the number of pixels not in the true target region (true background pixels).

The performance evaluation shows that, over large ranges of elevation and aspect angles, the use of polarization data improves segmentation accuracy significantly over the use of intensity (FLIR) data alone. The performance of the statistical segmentation and labeling algorithm was plotted as segmentation accuracy versus false detection rate. The points along curves correspond to different threshold values. As shown in Figure 14, there is a dramatic improvement in segmentation accuracy, as much as 55%, when using polarization data near the elevation angle of  $30^\circ$  and aspect angle of  $30^\circ$ . For the overhead view, the improvement is as large as 20%. However, for front, back, and broadside views, there is no improvement when using polarization data.

### **3.4. TARGET CLASSIFICATION ALGORITHM**

#### **3.4.1. CLASSIFICATION TECHNIQUES**

There are a number of ways that objects can be classified. Among these approaches, are feature-based methods and model-based techniques. In the feature-based methods, a relatively small set of features, capturing the unique characteristics of the targets, are extracted from the potential targets. Then they are compared with the stored sets of similar feature types that are associated with known targets of interest. A decision is made based on the statistical similarity of the two. In the model-based techniques, the classification is viewed as the output of two processes of hypothesis generation and hypothesis verification. Based on the sensory-derived object signature a set of hypothesis about the object labels will be generated. Then, for each hypothesis, use will be made of everything that is known about the target given that the hypothesis is true. This knowledge includes a physics-based model of the target under the existing scene and scenario. Then, this expected knowledge is searched and verified in the actual sensory-derived signature and a similarity measure is computed. This process will be performed for each hypothesis. This reasoning mechanism will continue until one achieves acceptable level of confidence in one or more hypothesis. The preference for the approach is dependent on a number of parameters, among them the availability of the models, number of pixels on targets, and computational requirements.

The approach that is pursued here is a model-based technique. The output of the Detection Module is fed to the Recognition Module that matches the edge map and the segmented regions with the stored polarization-sensitive models of the objects of interest. The recognition is performed in two ways. In one approach that was described previously, a statistical similarity measure (Fisher Criterion) is used to match the extracted target's with a library of stored prototypes. In another approach, an image correlator is used to correlate the stored models with the edge map and the segmented target regions. A correlation surface is obtained and then the correlation distances between the best matches corresponding to different object models are compared to decide on the best label for the unknown objects. Figure 15(a) shows a target model, the original sensory-derived images of Figure 12 with the polarization components represented as color. Figure 15(b) shows a portion of the tail of the missile. Figure

15(c) shows the resulting correlation surface with the position of the correct match. The arrow at the right inside the Figure 15(c) indicates the position of the highest peak.

### 3.4.2. PERFORMANCE EVALUATION OF CLASSIFICATION ALGORITHM

In the model-based recognition scheme, the sensory derived object was matched against a set of stored target models, and the maximum matching distance was tabulated. The sensory derived objects corresponded to views of the missile on a mobile launcher [Figure 12] seen from an elevation angle of 30 degrees and aspect angles of 0, 30, 90, 130, and 180 degrees. The resulting confusion matrix is shown in Tables 1–3.

Tables 1–3 show that the intensity I-only sensor data, i.e. FLIR images, cannot correctly classify among most of the target aspect angles. However, with a combination of percent of polarization P and angle of polarization  $\phi$ , all aspect angles were correctly classified (with the exception of 90 degrees: broadside view). This demonstrates that a combination of intensity and polarization data can provide a higher performance than the intensity data alone can provide. The bold numbers show the maximum value for each row.

Table 1. Confusion Matrix: Matching results for intensity I-only (FLIR).

	Model at 0° Aspect Angle	Model at 30° Aspect Angle	Model at 90° Aspect Angle	Model at 130° Aspect Angle	Model at 180° Aspect Angle
Sensory-derived Target at 0° Aspect Angle	0.915	0.754	0.817	0.799	<b>0.954</b>
Sensory-derived Target at 30° Aspect Angle	0.913	0.741	0.815	0.792	<b>0.954</b>
Sensory-derived Target at 90° Aspect Angle	0.919	0.750	0.841	0.797	<b>0.954</b>
Sensory-derived Target at 130° Aspect Angle	0.916	0.742	0.818	0.807	<b>0.953</b>
Sensory-derived Target at 180° Aspect Angle	0.917	0.742	0.815	0.790	<b>0.964</b>

Table 2. Confusion Matrix: Matching results for angle of polarization plane  $\phi$ -only.

	Model at 0° Aspect Angle	Model at 30° Aspect Angle	Model at 90° Aspect Angle	Model at 130° Aspect Angle	Model at 180° Aspect Angle
Sensory-derived Target at 0° Aspect Angle	<b>0.667</b>	0.488	0.204	0.546	0.511
Sensory-derived Target at 30° Aspect Angle	0.570	<b>0.642</b>	0.215	0.522	0.497
Sensory-derived Target at 90° Aspect Angle	<b>0.599</b>	0.499	0.216	0.550	0.460
Sensory-derived Target at 130° Aspect Angle	0.568	0.510	0.232	<b>0.675</b>	0.477
Sensory-derived Target at 180° Aspect Angle	<b>0.585</b>	0.499	0.207	0.547	0.524

Table 3. Confusion Matrix: Matching results for percent of polarization P-only.

	Model at 0° Aspect Angle	Model at 30° Aspect Angle	Model at 90° Aspect Angle	Model at 130° Aspect Angle	Model at 180° Aspect Angle
Sensory-derived Target at 0° Aspect Angle	<b>0.836</b>	0.627	0.542	0.630	0.785
Sensory-derived Target at 30° Aspect Angle	<b>0.788</b>	0.653	0.542	0.629	0.776
Sensory-derived Target at 90° Aspect Angle	<b>0.782</b>	0.623	0.583	0.616	0.774
Sensory-derived Target at 130° Aspect Angle	<b>0.786</b>	0.619	0.544	0.638	0.774
Sensory-derived Target at 180° Aspect Angle	0.794	0.620	0.541	0.627	<b>0.823</b>

#### 4. SUMMARY

Two methods have been described, where intensity and polarization images are captured and processed into images of the target's temperature distribution and the target's three-dimensional shape and orientation. In the first method, a single video frame is captured and processed into images of temperature and shape. In the second method, microscanning is used and three video frames are captured and processed into images of temperature and shape with higher resolution. The first method would require almost no changes to the optics and

mechanical structure of existing sensors employing focal plane arrays. When shape and temperature are varying, the polarization-sensitive thermal imaging sensor will be able to capture these changes in real time. With high-speed signal processing, high-resolution polarimetric data can be captured and displayed at video frequency.

In order to extend the sensor's capabilities to image all four Stokes parameters I, Q, U, and V, we are developing novel microscale retarder arrays. These retarders will be combined with linear polarizers in an imaging sensor. This sensor will be able to capture images of the four Stokes parameters in real time and without mechanically moving parts. Each retarder is a composite of surface-relief gratings. We have demonstrated, by calculation, that, with the proper dimensions and orientation, the composite retarder is highly achromatic and has a large field angle.

Polarimetric imaging is often proposed as a technique to improve target detection and recognition. We have demonstrated, using a limited set of synthetic imagery, a significant improvement in the performance of automatic target detection, segmentation, and classification algorithms when processing polarimetric images compared to FLIR images.

## ACKNOWLEDGMENTS

We express our appreciation to our sponsors who have supported this work in the past under NASA contract NAS9-19115, Navy contract N68936-96-C-0185, and Air Force contract F30602-94-C-0152. Special thanks to our sponsor Dr. Gracie E. Davis at the Defense Threat Reduction Agency who supports our work under BMDO contract DSWA01-98-M-0207.

## REFERENCES

- <sup>1</sup> C.S.L. Chun, D.L. Fleming, and E.J. Torok, "Polarization-sensitive, thermal imaging," in *Automatic Object Recognition IV*, Firooz A. Sadjadi, Editor, Proc. SPIE 2234, 275-286 (1994).
- <sup>2</sup> C.S.L. Chun, D.L. Fleming, W.A. Harvey, and E.J. Torok, "Polarization-sensitive thermal imaging sensors for target discrimination," in *Targets and Backgrounds: Characterization and Representation IV*, Wendell R. Watkins and Dieter Clement, Editors, Proc. SPIE 3375 (1998).
- <sup>3</sup> M.G. Destriau et al., "Réalisation d'un quart d'onde quasi achromatique par juxtaposition de deux lames cristallines de même nature," in *J. Phys. Radium* 10(2), 53-55 (1949)
- <sup>4</sup> R.A. Chipman, "Polarimetry," in the *Handbook of Optics*, 2<sup>nd</sup> ed., vol II, Chapt. 22, M. Bass, ed., (McGraw Hill / OSA, 1994).
- <sup>5</sup> A. Yariv and P. Yeh, "Electromagnetic propagation in periodic stratified media. II. Birefringence, phase matching, and x-ray lasers," *J. Opt. Soc. Am.* 67(4) 438-448 (1977).
- <sup>6</sup> C.S.L. Chun, F. A. Sadjadi, and D. Ferris, "Automatic target recognition using polarization-sensitive, thermal imaging," in *Automatic Object Recognition V*, Firooz A. Sadjadi, Editor, Proc. SPIE 2485 (1995).

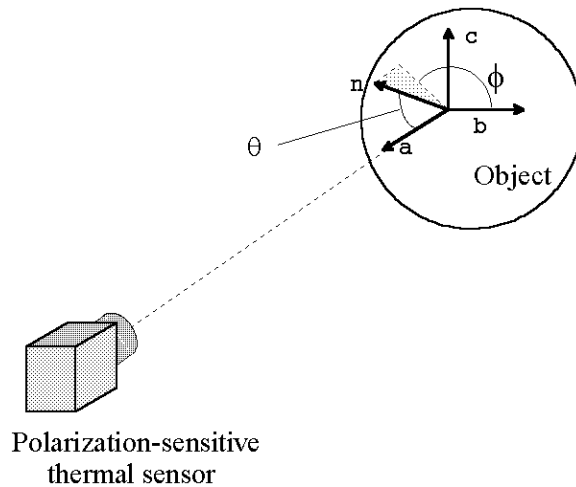


Figure 1. Thermal radiation from the surface of an object contains information about the object's shape. By sensing polarization data from a point on the surface, the orientation of the surface element can be derived. The normal vector to the surface element is  $\mathbf{n}$  which is defined by the angles  $\theta$  and  $\phi$ .  $\phi$  is imaged directly.  $\theta$  is calculated from the image of the percent of polarization  $P$ .

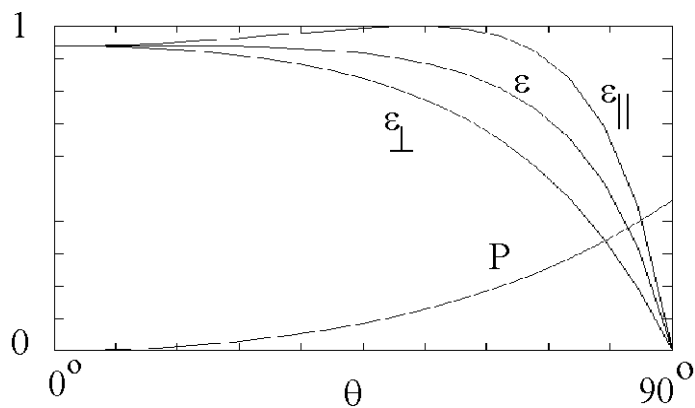


Figure 2. For most materials, the percent of polarization  $P$  increases as the radiation is emitted at a more grazing angle, that is at greater  $\theta$ .

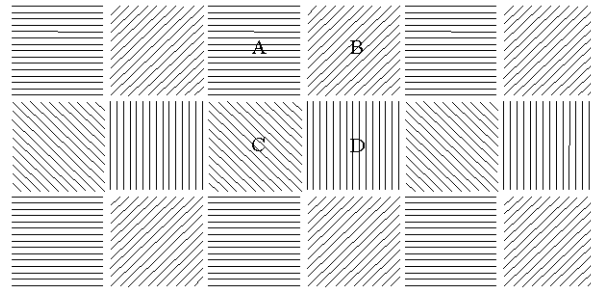


Figure 3. Physics Innovations Inc. has developed a polarization-sensitive thermal imaging sensor. In this sensor each detector element of a focal plane array has its own polarizer and the polarizer orientations are rotated from element to element. The polarizers are wire grids formed by microlithography on a substrate.

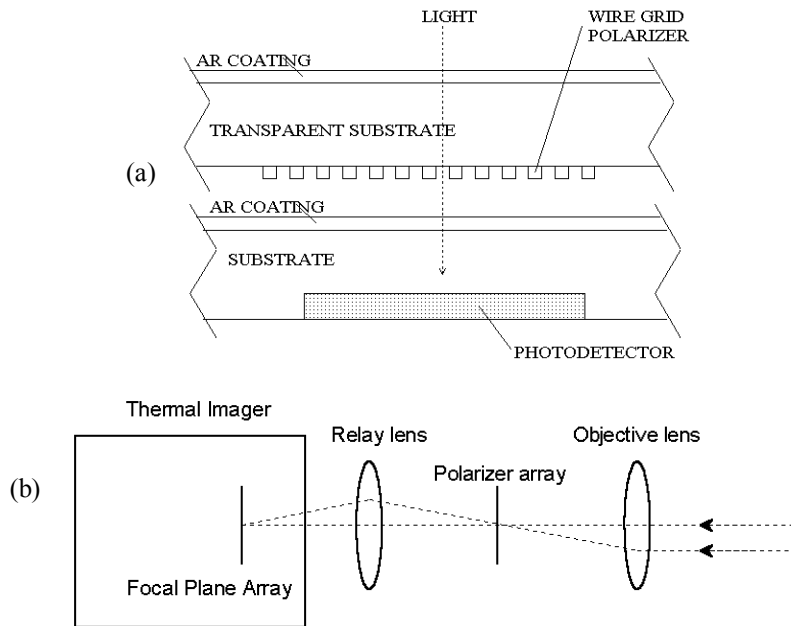
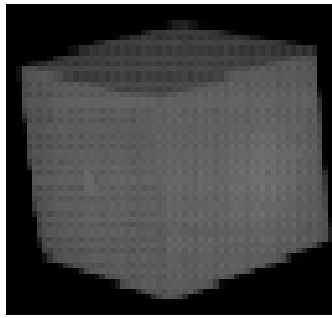
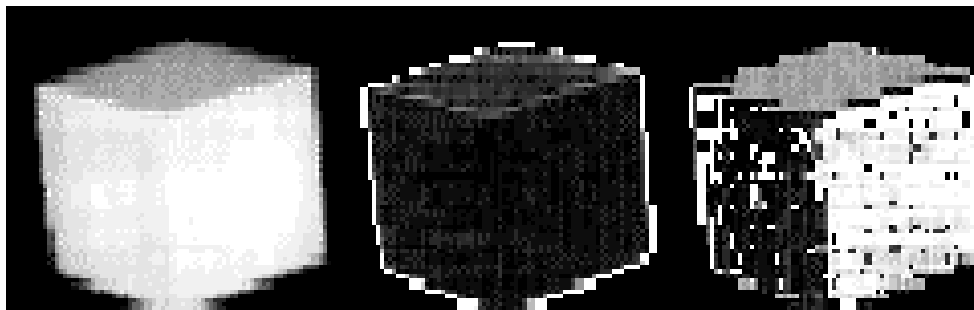


Figure 4. Two methods for integrating the polarizer array and focal plane array. (a) Wire grid polarizers can be integrated with photodiode arrays by placing the polarizers on a substrate in close proximity to the photodiode array. (b) A schematic diagram of the polarization-sensitive, thermal imaging sensor. Radiation from the target is imaged by an objective lens onto the polarizer array. Light which is transmitted by the polarizer array is imaged by a relay lens onto the photodetector array.



Single video frame



Intensity

Percent of  
Polarization P

Angle of  
Polarization  $\phi$

Figure 5. The object is a heated cube. Images of three Stokes parameters, calculated from a single video frame. These I, P, and  $\phi$  images demonstrate that the three-dimensional shape of a target and the target's temperature distribution can be obtained simultaneously using polarization-sensitive thermal imaging.

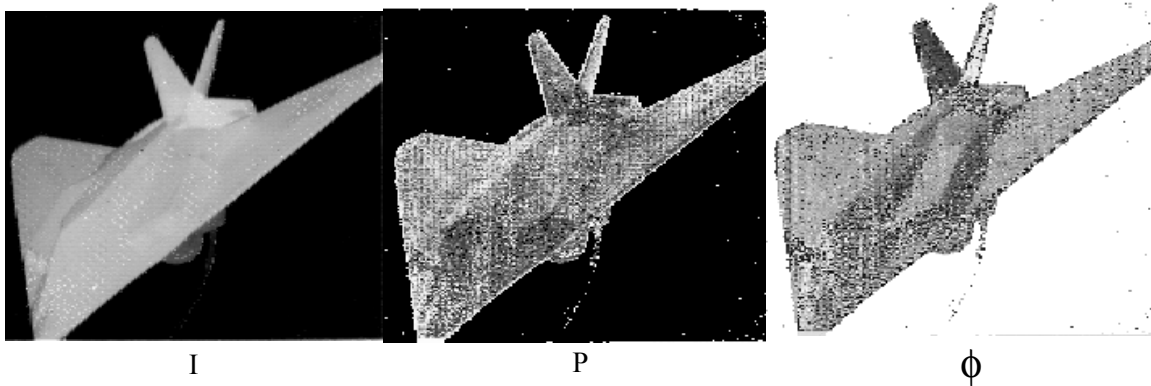
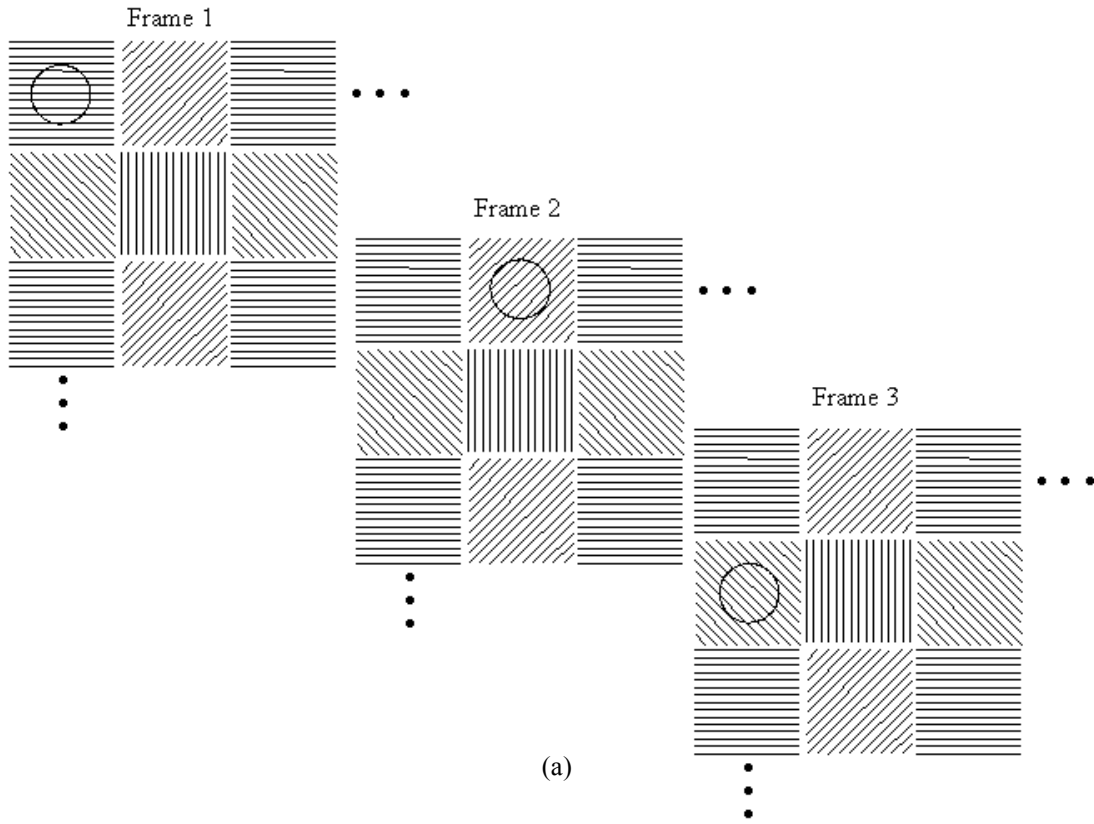
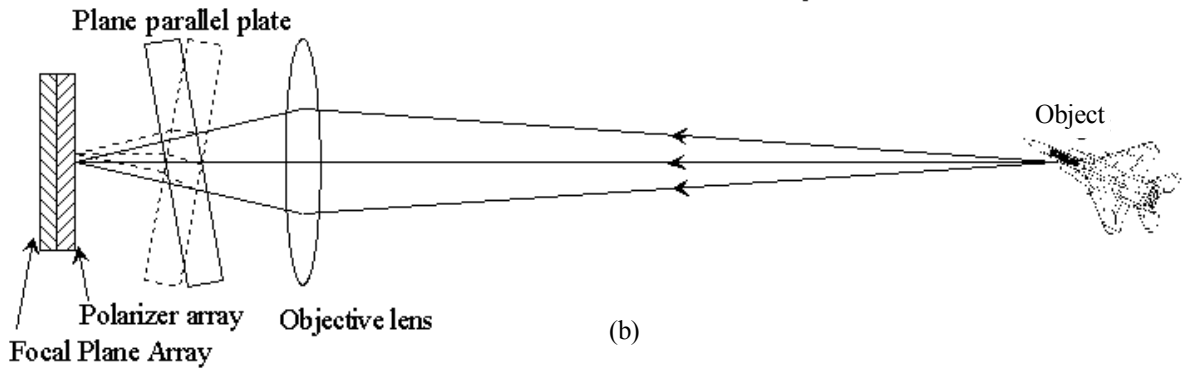


Figure 6. High-resolution polarization image of a scale model of an aircraft. High-resolution was achieved by using a microscanning technique described in Figure 7.



(a)



(b)

Figure 7. The sensor shown in Figure 4(b) was improved with higher resolution and the ability to resolve polarimetric data from a point source, e.g. targets at long range. This improvement uses the technique of microscanning. (a) In three successive video frames, the image on the polarizer array is displaced horizontally and vertically. The circle represents the image of a point source. By combining Frames 1, 2 and 3, the three parameters  $I$ ,  $P$  and  $\phi$  can be determined for the point source.  $I$ ,  $P$ , and  $\phi$  can be captured and displayed at video frequency. (b) The image can be microscanned by tilting a plane parallel plate in the optical path about vertical and horizontal axes.

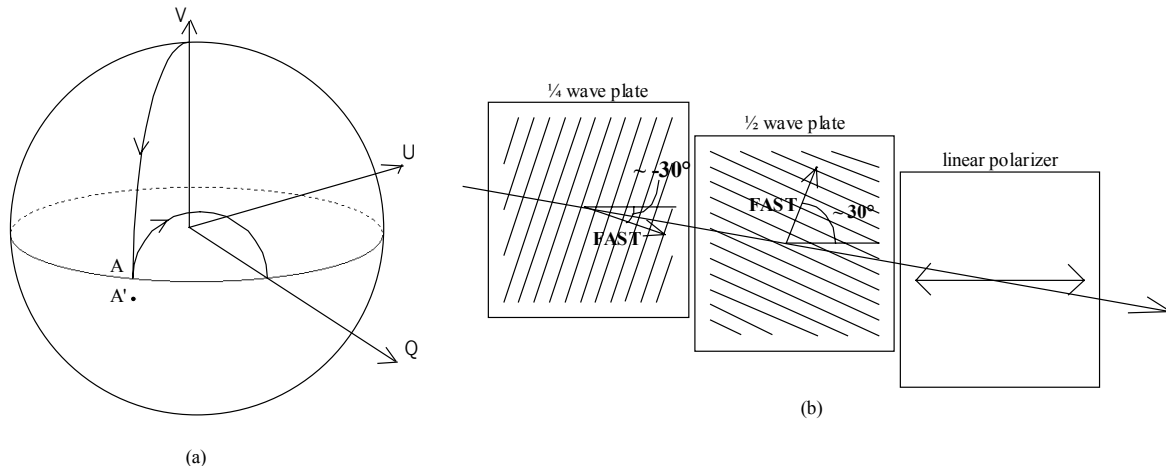


Figure 8. A well-established method for constructing an achromatic quarter-wave retarder is to use a combination of a quarter-wave waveplate followed a half-wave waveplate. (a) This Poincaré sphere representation shows how the composite retarder transforms circularly polarized light V to linearly polarized light Q. (b) In a pixel of the 4-Stokes-parameter imaging sensor, a composite retarder will be combined with a linear polarizer.

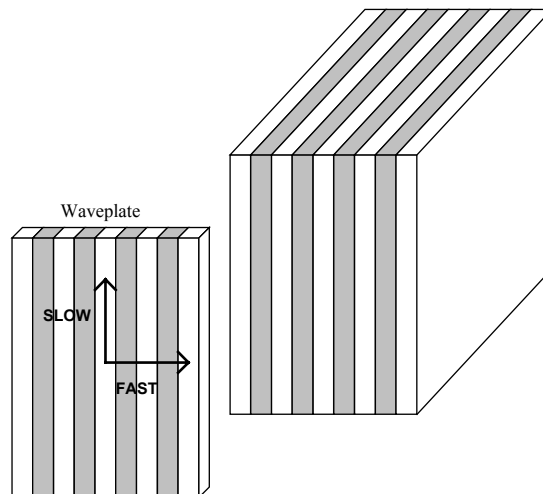


Figure 9. . A surface-relief grating is a series of identical parallel linear ridges arranged on a planar substrate. The grating can be seen to have form birefringence by considering the grating as a thin slice of a periodic stratified material. These gratings can be used to form a waveplate array in the 4-Stokes-parameter imaging sensor [Figure 10].

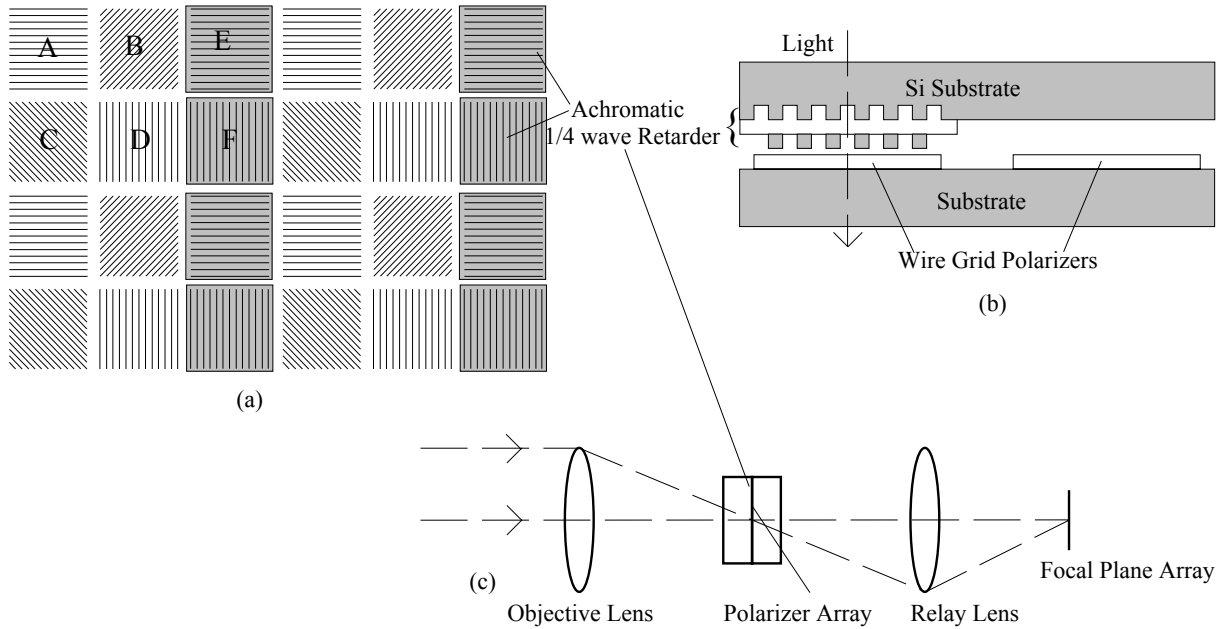


Figure 10. A wide-band sensor for imaging four Stokes parameters. (a) A retarder array can be combined with a polarizer array. (b) The retarder array will contain elements which are achromatic quarter-wave retarders. Stokes vector images can be captured using the arrangement shown in (c). The retarder array and polarizer array are placed at the focus of an objective lens. Light which is transmitted by the arrays is focused onto a focal plane array using a relay lens.

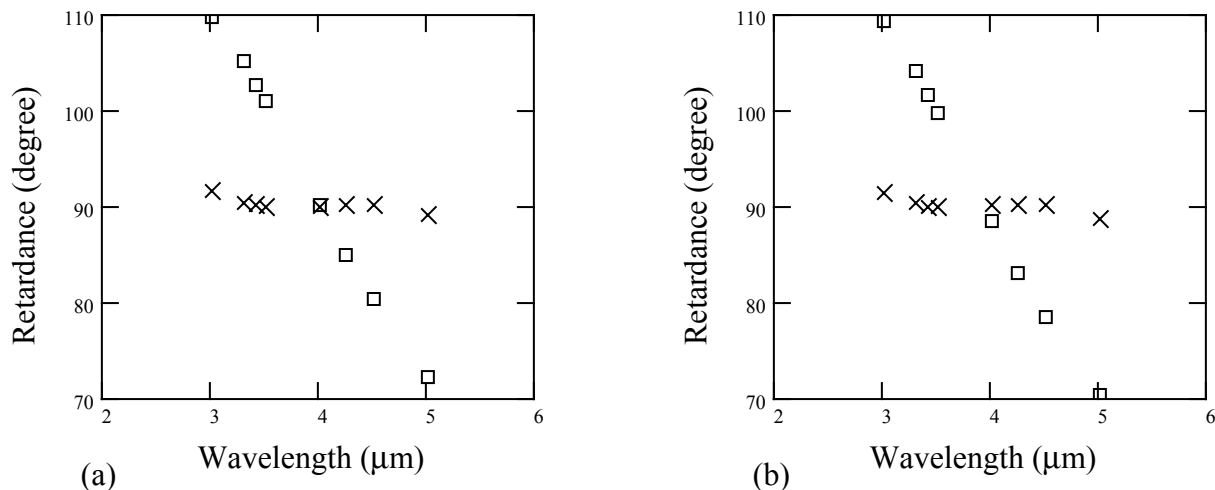


Figure 11. (a) Retardance for a single  $\frac{1}{4}$ -wave waveplate ( $\square$ ) and for the composite retarder ( $\times$ ) at normal incidence. (b) Retardance at incidence angle  $22.6^\circ$  from normal. These results show that, in the wavelength range 3–5  $\mu\text{m}$ , the retardance of the composite retarder is nearly independent of wavelength and varies negligibly over field angles subtended by a low  $f/\#$  lens.

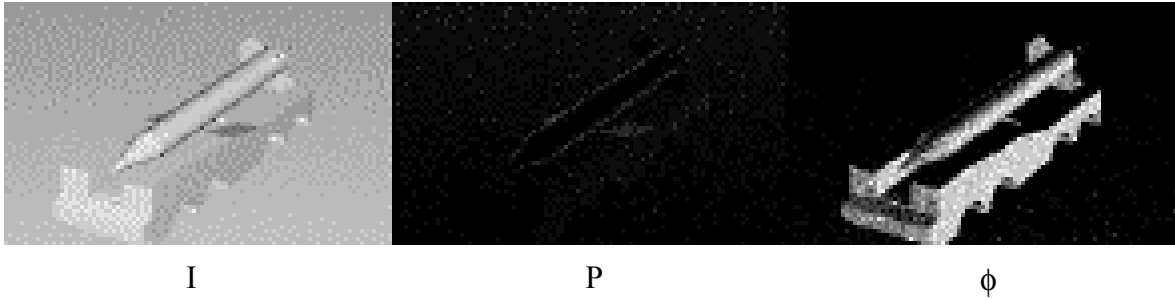


Figure 12. For our study of automatic target detection algorithms, a polarization ray tracer was used to generate the sensor images. The sensor images include the characteristics of a typical PtSi focal plane array camera. The image has three components, intensity  $I$  (same as FLIR), percent of polarization  $P$ , and angle of polarization  $\phi$ .

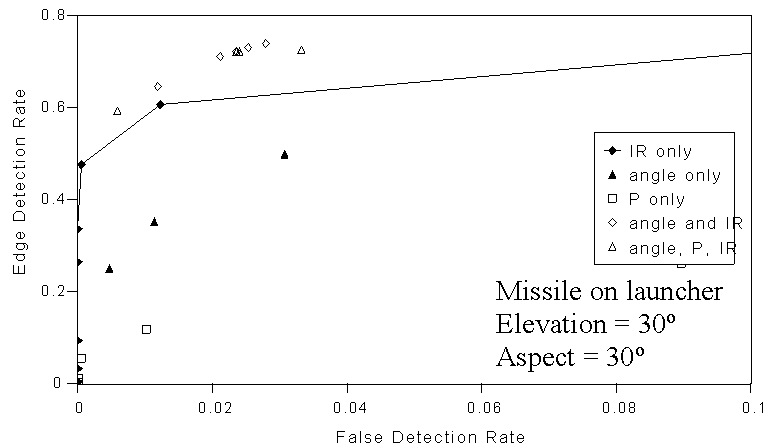


Figure 13. The performance of the Sobel operator on the sensor images is summarized using receiver-operating-characteristics (ROC) curves

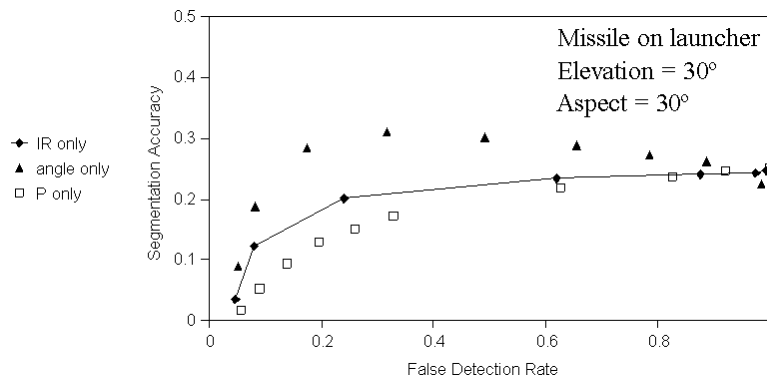


Figure 14. The performance of the statistical segmentation and labeling algorithm is measured by the segmentation accuracy and false detection rate.

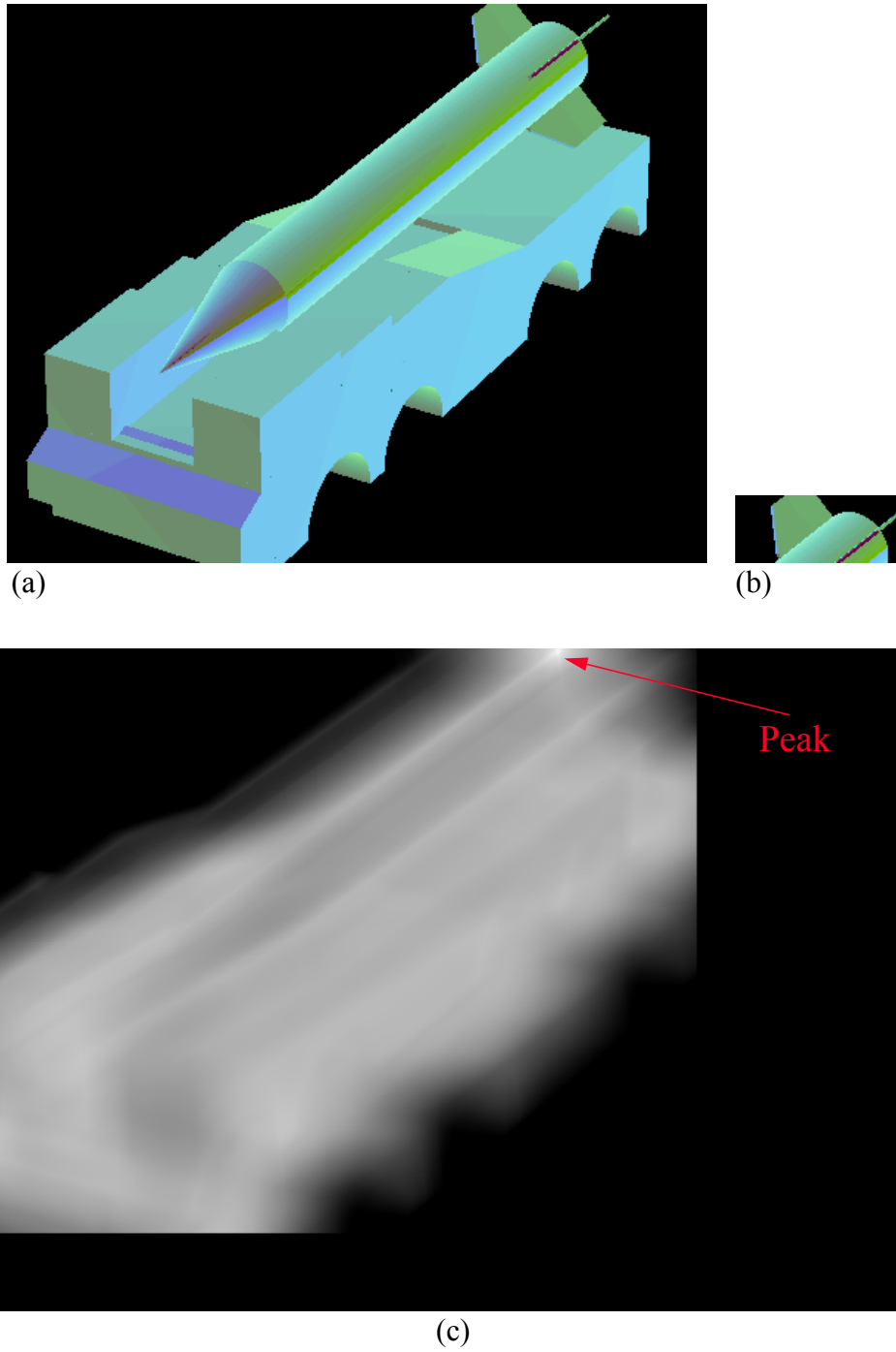


Figure 15. (a) The original sensory-derived images of Figure 12 with the polarization components represented as color. (b) A portion of the tail of the missile. (c) The resulting correlation surface with the position of the correct match indicated with an arrow.